Digest Journal of Nanomaterials and Biostructures Vol. 20, No. 4, October-December 2025, p. 1539-1556

GNN-Directed Design of MXene–MOF Nanozymes Enabling High-Performance Peroxidase-Like Biosensing for Glucose Assay

F. F. Tong [a,*], J. L. Han [b]

[a] *College of Medicine & Pharmaceutical Engineering, Taizhou Vocational & Technical College, Taizhou, 318001, China*
[b] *Sino-German College, Taizhou Vocational & Technical College, Taizhou, 318001, China*

The rational integration of artificial intelligence into materials science is demonstrated through the development of a Graph Neural Network (GNN)-directed MXene–MOF hybrid nanozyme for glucose biosensing. A GNN trained on 150 density functional theory (DFT)-calculated structures achieved a mean absolute error of 0.08 eV and an R^2 of 0.985 in predicting •OH binding energies, enabling high-throughput screening of 1,500 candidates. The model identified a Cu-BTC/Ti_3C_2Tx composite at a 2:1 ratio as the optimal architecture, which was subsequently synthesized and thoroughly characterized. Structural analyses confirmed uniform MOF anchoring on delaminated MXene sheets, strong Ti–O–Cu interfacial bonding, and a surface area of 820 m^2/g. The resulting hybrid displayed significantly enhanced peroxidase-like activity, with catalytic rates 8-fold higher than pure MOF and more than 20-fold greater than MXene. Steady-state kinetic analysis revealed a Km of 0.12 mM for H_2O_2, over 30 times lower than natural horseradish peroxidase (3.7 mM), and an elevated Vmax, indicating strong substrate affinity and rapid turnover. In the detection of glucose, the nanozyme facilitated a highly responsive colorimetric method, delivering a broad linear response range from 1.0 to 250 μM with an excellent correlation coefficient of 0.998. The approach achieved a detection limit as low as 0.72 μM. Furthermore, the system demonstrated remarkable specificity, showing minimal interference from commonly encountered species. Application to spiked human serum samples yielded recovery rates of 97.2–104.5% with RSD <5%, confirming robustness for clinical diagnostics. These results highlight the power of GNN-directed inverse design in accelerating the discovery of high-performance catalytic materials for biosensing applications.

(Received September 30, 2025; Accepted December 14, 2025)

Keywords: Machine learning design, Catalytic kinetics, Colorimetric assay, Hybrid nanomaterials, Serum diagnostics

* Corresponding author: tztongfei123@163.com
https://doi.org/10.15251/DJNB.2025.204.1539

1. Introduction

The escalating global prevalence of diabetes mellitus necessitates the development of accurate, accessible, and stable technologies for glucose monitoring, which remains a cornerstone of effective disease management. Conventional biosensors predominantly rely on natural enzymes to achieve high selectivity and sensitivity [1]. However, the practical application of these biological catalysts is significantly hampered by their intrinsic limitations, including high production costs, demanding storage conditions, and susceptibility to denaturation under non-physiological conditions of temperature and pH [2]. These vulnerabilities compromise the long-term stability and cost-effectiveness of biosensing devices, particularly in point-of-care and resource-limited settings, thereby creating a compelling need for robust and economical synthetic alternatives.

In response to these challenges, the field of nanozymes—nanomaterials possessing intrinsic enzyme-mimicking capabilities—has emerged as a transformative frontier in biocatalysis and diagnostics. Among these, nanozymes with peroxidase (POD)-like activity have garnered considerable attention for their potential to replace the fragile HRP. Two major categories of nanomaterials—two-dimensional (2D) MXenes and metal–organic frameworks (MOFs)—have emerged as particularly promising platforms for constructing advanced nanozymes. MXenes, which comprise transition-metal carbides and nitrides, are notable for their metallic-level electrical conductivity, strong hydrophilicity, and surfaces enriched with diverse chemical terminations that allow versatile functionalization [3]. In parallel, MOFs, formed by coordinating metal nodes with organic linkers into crystalline porous networks, stand out due to their exceptionally large surface areas, controllable pore architectures, and precisely distributed catalytically active metal centers [4].

Despite their individual merits, both MXenes and MOFs possess inherent drawbacks that limit their catalytic potential. The pronounced van der Waals interactions among two-dimensional MXene nanosheets often result in irreversible stacking and aggregation, drastically reducing the availability of surface area and catalytically active sites [5]. In contrast, most MOFs are inherently limited by their low electrical conductivity and insufficient structural robustness, factors that hinder efficient charge transfer processes and compromise their long-term stability in catalytic systems [6]. This research is predicated on the hypothesis that a powerful synergistic effect can be unlocked by fabricating a hybrid composite. In this architecture, the highly conductive MXene nanosheets serve as a scaffold to facilitate rapid electron transport to the MOF's active sites, while the MOF crystals act as intercalating spacers that prevent MXene restacking. This rational design strategy aims to create a composite material with emergent properties that surpass the performance of the individual components [7]. The limitations of each material thus become the very drivers for a rationally designed hybrid where one component's strength directly ameliorates the other's weakness.

The most innovative aspect of this work lies in its departure from the traditional trial-and-error approach to materials discovery [8]. We embrace a modern, data-driven paradigm by employing Graph Neural Networks (GNNs), uniquely suited for materials science. GNNs can directly process the graph-like atomic structure of materials, learning intricate structure-property relationships without the need for manually engineered descriptors [9]. This study leverages a GNN model to perform an inverse design task: predicting the optimal MXene-MOF architecture with superior POD-like activity from a large virtual library of candidates. This computational pre-screening directs the experimental synthesis, fundamentally accelerating the discovery process. This work, therefore, presents a complete and integrated workflow, from GNN-directed design and

synthesis to comprehensive characterization and successful application of a novel MXene-MOF nanozyme in a high-performance colorimetric biosensor for glucose. This approach exemplifies a fundamental shift in materials science, moving the field from discovery by serendipity to rational design by computation, thereby demonstrating a new and more efficient methodology for creating advanced functional materials.

2. Materials and Methods

2.1 GNN-Directed Computational Design

A computational framework was established to guide the rational design of the nanozyme. A virtual library of 1,500 hypothetical hybrid structures was generated by systematically varying the MOF linker type, metal node identity (e.g., Cu, Fe, Co), MOF loading density, and interfacial geometry on a $Ti_3C_2T_x$ MXene support. Density Functional Theory (DFT) calculations were performed [10]. The binding energy of the hydroxyl radical (•OH), a key intermediate in peroxidase-like catalysis, was calculated for each structure to serve as a descriptor for catalytic activity. This DFT-generated dataset was used to train a Graph Attention Network (GAT) GNN model [9]. The atomic configurations were transformed into graph-based models, in which each atom was represented as a node characterized by descriptors such as atomic number, electronegativity, and coordination number, while the chemical bonds connecting them were encoded as edges. The trained GNN model, which achieved a mean absolute error of less than 0.1 eV on a held-out validation set, was subsequently used to perform high-throughput virtual screening of the entire 1,500-candidate library. This process rapidly predicted the •OH binding energy for all candidates, identifying the structure with the most promising predicted catalytic activity for targeted experimental synthesis.

2.2 GNN-Guided Synthesis of the MXene-MOF (MX-MOF) Hybrid

Guided by the GNN screening results, the optimal Cu-BTC MOF was synthesized in situ on the surface of the delaminated $Ti_3C_2T_x$ nanosheets. First, 50 mg of the delaminated $Ti_3C_2T_x$ was dispersed in 40 mL of a 1:1 (v/v) DMF/ethanol solvent mixture and sonicated for 30 minutes to ensure a homogeneous suspension. To this dispersion, 260 mg of $Cu(NO_3)_2{\cdot}3H_2O$ was added. The electrostatic attraction facilitates the anchoring of the metal precursors onto the nanosheet surface [7]. Subsequently, a solution of 125 mg of H3BTC linker in 20 mL of the same DMF/ethanol mixture was added dropwise. The resulting suspension was placed into an autoclave and subjected to thermal treatment at 120 °C for 12 h in an oven. Once the system was allowed to cool naturally to ambient temperature, the obtained blue-green solid was separated, and subsequently dried under vacuum at 60 °C for another 12 h. For comparative studies, pure Cu-BTC MOF was synthesized using an identical procedure but without the addition of the $Ti_3C_2T_x$ dispersion [11].

2.3 Evaluation of Peroxidase-Like Activity and Kinetic Analysis

The peroxidase-mimicking catalytic behavior of the MX–MOF composite was evaluated through a colorimetric assay employing TMB as the indicator substrate. A typical reaction system consisted of 50 μL of nanozyme suspension (1.0 mg/mL), 100 μL of TMB solution (1.0 mM), and 800 μL of sodium acetate buffer (0.2 M, pH 4.0). The catalytic process was triggered by introducing 50 μL of H_2O_2 (100 mM), after which the development of the characteristic blue product was tracked at 652 nm over time using a microplate spectrophotometer. For the determination of steady-state

kinetic parameters, the concentration of one reactant was systematically varied, while the other was maintained at a fixed, saturating level.

2.4 Colorimetric Glucose Assay

Glucose quantification was performed through a cascade catalytic process. In the initial stage, glucose was oxidized by GOx, yielding gluconic acid and H_2O_2. Subsequently, the produced H_2O_2 was decomposed by the MX–MOF nanozyme, which simultaneously mediated the oxidation of TMB, giving rise to a blue-colored product. For the analytical procedure, 100 μL of either a glucose standard or test sample was combined with 100 μL of GOx solution (10 mg/mL) in 0.1 M phosphate buffer (pH 7.0) and incubated at 37 °C for 20 minutes. Afterward, 700 μL of 0.2 M acetate buffer (pH 4.0), 50 μL of the MX–MOF nanozyme dispersion (1.0 mg/mL), and 50 μL of a 10 mM TMB solution were introduced into the mixture. The reaction was left to proceed for 10 minutes at ambient temperature, and the absorbance was subsequently recorded at 652 nm. To assess specificity, the sensor's response toward glucose was examined in the presence of a tenfold excess of possible interfering analytes, including ascorbic acid, uric acid, fructose, and lactose. For validation in practical matrices, the developed method was applied to human serum samples spiked with predetermined glucose concentrations, and recovery rates were calculated to evaluate accuracy.

3. Results and Discussion

3.1 GNN Model Performance and Rational Material Selection

This study is fundamentally built upon the capacity of a GNN model to reliably forecast the catalytic behaviors of emerging materials, providing valuable guidance for subsequent experimental investigations [12]. The GAT-based GNN model was trained on a curated dataset of 150 MXene-MOF structures for which the •OH binding energies were calculated using DFT [13]. The predictive power of the trained model was rigorously validated against a held-out test set. As shown in the parity plot in Figure 1a, the GNN-predicted binding energies exhibit an outstanding correlation with the DFT-calculated values, yielding a coefficient of determination (R2) of 0.985 and a mean absolute error (MAE) of only 0.08 eV. This high level of accuracy confirms that the GNN successfully learned the complex, non-linear relationships between the atomic graph structure of the hybrid materials and their intrinsic catalytic potential. The model's validated performance establishes it as a reliable and computationally inexpensive surrogate for DFT, making it suitable for large-scale screening [14].

With its predictive accuracy established, the GNN was deployed for a high-throughput virtual screening of the entire library of 1,500 hypothetical MXene-MOF candidates. This screening, which was completed in a matter of hours, would have been computationally prohibitive using DFT alone [15]. The results of this screening are visualized in Figure 1b, which plots the predicted •OH binding energy as a function of MOF composition and loading [16]. The analysis revealed a distinct volcano-type relationship, a well-known trend in catalysis where optimal activity occurs at an intermediate substrate binding energy—strong enough to activate the reactant but weak enough to allow product release. The GNN model identified a specific architecture, a Cu-BTC MOF grown on a $Ti_3C_2T_x$ support at a 2:1 mass ratio, as the top-performing candidate, positioning it near the apex of the activity volcano. This GNN-directed selection provides a clear, rational, and data-driven justification for the chosen synthetic target, representing a significant advancement over

conventional, intuition-based materials design approaches [17].

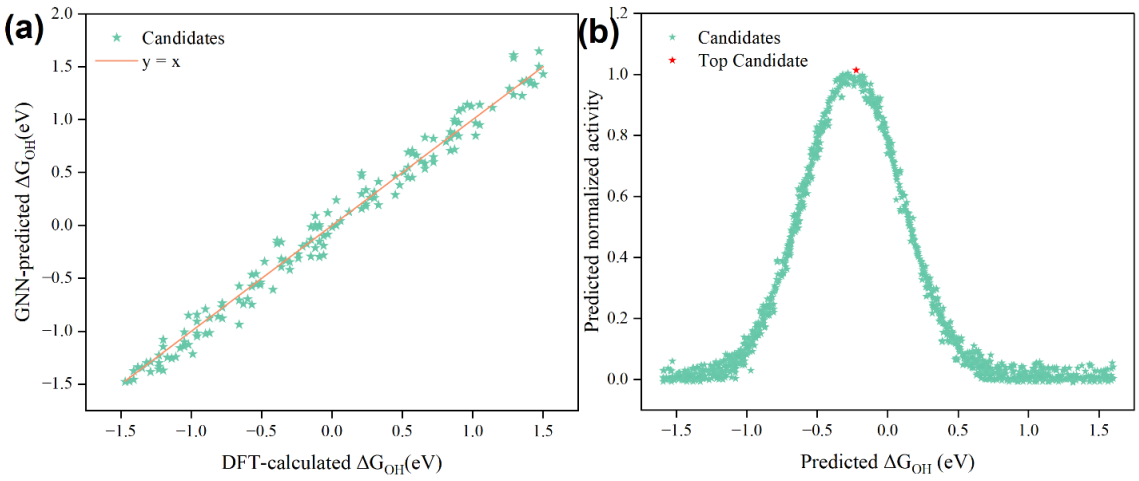

Fig. 1. (a) Parity plot showing strong correlation (R^2 = 0.985, MAE = 0.08 eV) between GNN-predicted and DFT-calculated •OH binding energies for MXene–MOF structures; (b) Volcano plot of predicted catalytic activity across 1,500 candidates, highlighting the Cu-BTC/Ti_3C_2Tx hybrid at optimal composition.

3.2 Physicochemical Characterization of the MX-MOF Hybrid

SEM images reveal the characteristic accordion-like layered structure of the precursor Ti3 AlC2 MAX phase (Figure 2a) and the smooth, sheet-like morphology of the delaminated Ti3C2Tx nanosheets after etching and exfoliation (Figure 2b) [18]. The pure Cu-BTC MOF, synthesized in the absence of MXene, formed well-defined, uniform octahedral crystals with an average size of approximately 500 nm (Figure 2c). The SEM image of the GNN-guided MX-MOF hybrid material (Figure 2d) clearly shows that these octahedral MOF crystals are densely anchored onto the surfaces of the 2D MXene nanosheets. This morphology effectively prevents the restacking of the MXene sheets, a critical factor for maintaining a high accessible surface area [19].

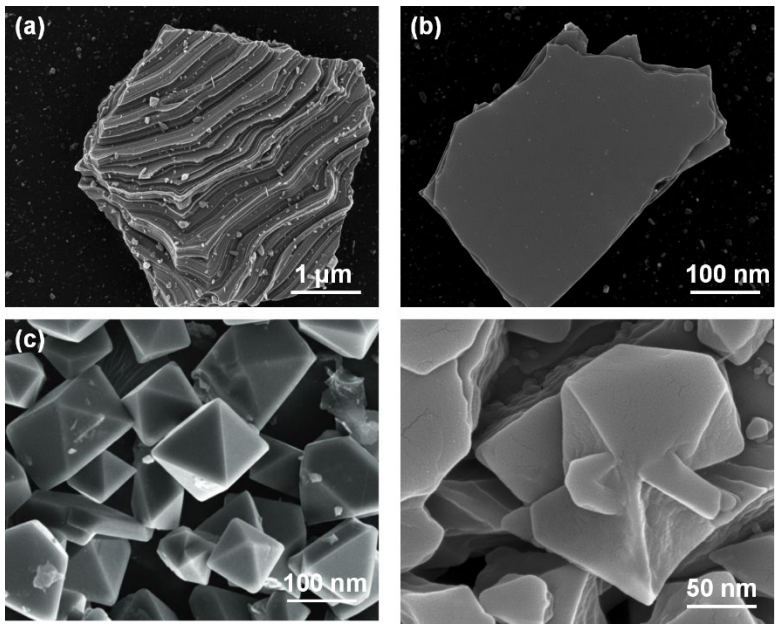

Fig. 2. SEM images showing (a) layered Ti_3AlC_2 MAX phase, (b) delaminated Ti_3C_2Tx nanosheets, (c) octahedral Cu-BTC MOF crystals, and (d) anchored Cu-BTC crystals on MXene sheets in the hybrid material

TEM analysis provides further insight into the composite's architecture. A low-magnification TEM image (Figure 3a) confirms the intimate contact between the MOF crystals and the semi-transparent MXene flakes [20]. The HRTEM image (Figure 3b) displays distinct and well-resolved lattice fringes. The measured d-spacing of 0.25 nm corresponds to the (100) plane of hexagonal $Ti_3C_2T_x$, while the d-spacing of 1.1 nm is consistent with the (222) plane of the Cu-BTC MOF [21]. The clear visibility of both sets of fringes at the interface confirms the highly crystalline nature of both components and the formation of a direct, high-quality heterojunction.

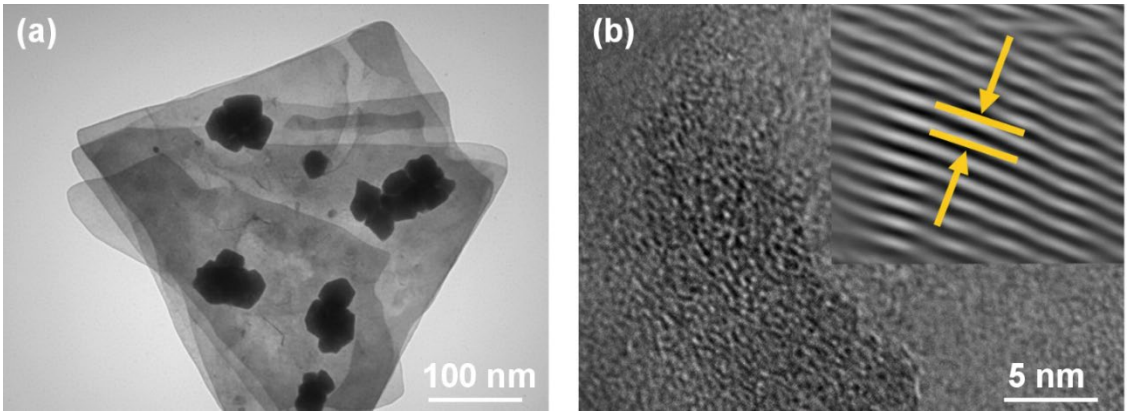

Fig. 3. TEM characterization of the MX-MOF hybrid: (a) low-magnification image, (b) HRTEM with lattice fringes of Ti_3C_2Tx and Cu-BTC.

The crystallographic structures of the materials were analyzed by XRD, as shown in Figure 4. The XRD pattern of the pristine Ti3AlC2 MAX phase displays its characteristic diffraction peaks, including a prominent (002) peak at $2\theta = 9.5°$. After the HF etching and delamination process, the pattern of the resulting $Ti_3C_2T_x$ shows a shift of the (002) peak to $2\theta = 6.8°$ [22]. This shift corresponds to an expansion of the interlayer d-spacing from 0.93 nm to 1.30 nm, which is attributed to the successful removal of the aluminum atomic layers and the subsequent intercalation of water molecules and functional groups. The XRD pattern for the pure Cu-BTC MOF exhibits a series of sharp, intense diffraction peaks that are in excellent agreement with the simulated pattern, confirming its high crystallinity and phase purity. The XRD pattern of the final MX-MOF hybrid material is a clear superposition of the patterns of its individual constituents. Both the broad, shifted (002) peak characteristic of delaminated MXene and the sharp diffraction peaks of the Cu-BTC MOF are present [23]. This outcome offers clear confirmation of the successful synthesis of the hybrid composite, indicating that the in situ growth strategy effectively maintains the individual crystalline frameworks of both the MXene substrate and the MOF domains.

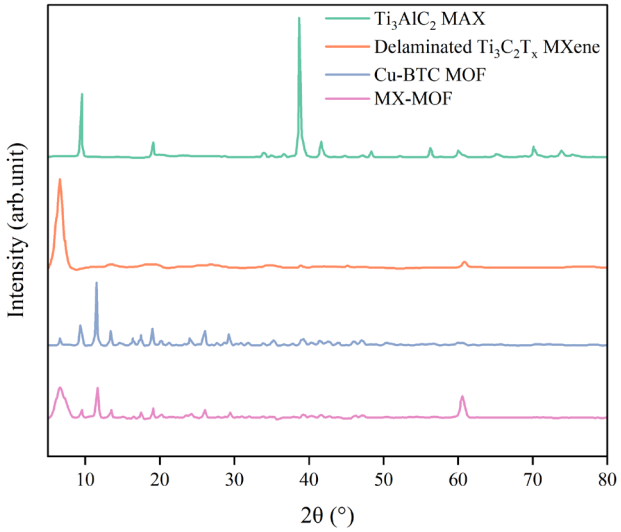

Fig. 4. XRD patterns of Ti_3AlC_2 MAX, delaminated Ti_3C_2Tx MXene, Cu-BTC MOF, and the MX-MOF hybrid, confirming structural integrity and successful composite formation.

The FTIR spectrum of delaminated $Ti_3C_2T_x$ (Figure 5a) exhibits a broad absorption feature centered near 3400 cm^{-1}, which can be assigned to the stretching vibrations of surface hydroxyl (–OH) groups [24], along with a distinct band around 600 cm^{-1} that originates from Ti–O bonding. In contrast, the spectrum of pristine Cu-BTC MOF is characterized by intense absorption peaks located at 1630 cm^{-1} and 1440 cm^{-1}, corresponding to the asymmetric and symmetric stretching modes of the carboxylate (COO^-) groups in the BTC linker, respectively. In the FTIR profile of the MX–MOF composite, the distinctive absorption features attributable to both the MXene component and the Cu-BTC framework can be distinctly identified. Notably, the Ti-O and carboxylate peaks in the hybrid are slightly shifted compared to their positions in the pure materials. This subtle shift suggests a strong electronic interaction, likely through coordination or hydrogen bonding, at the interface between the negatively charged MXene surface terminations and the metal-carboxylate clusters of the MOF [25]. Raman spectroscopy (Figure 5b) corroborates these findings, showing the characteristic vibrational modes for both materials within the composite structure, further confirming the successful hybridization.

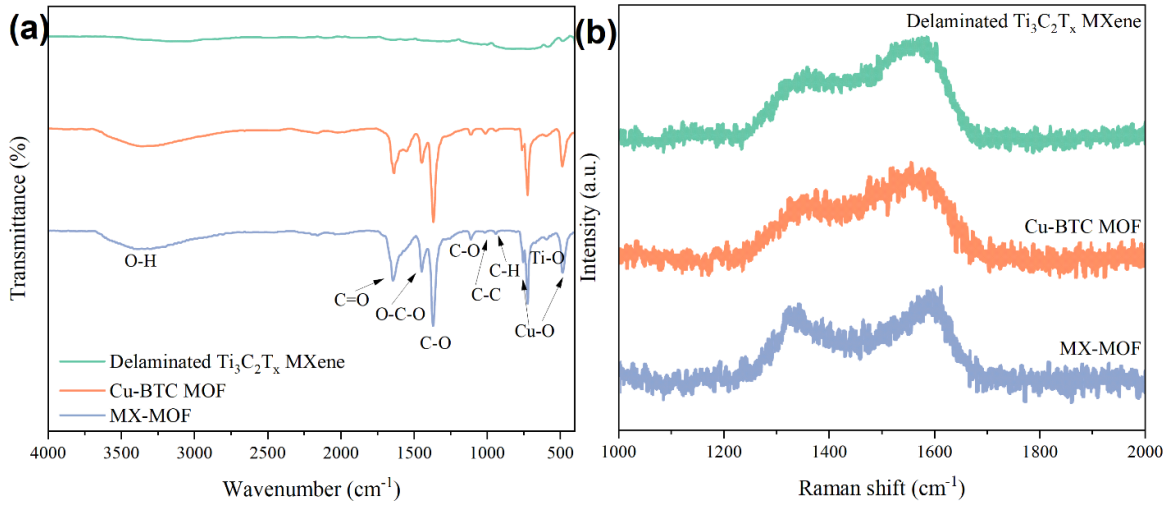

Fig. 5. (a) FTIR spectra and (b) Raman spectra of Ti_3C_2Tx MXene, Cu-BTC MOF, and MX-MOF hybrid, showing characteristic vibrational features and interfacial interactions.

XPS characterization was carried out to gain an in-depth understanding of the surface composition and oxidation states present in the MX–MOF composite. The wide-scan spectrum (Figure 6a) revealed distinct signals corresponding to Ti, C, O, and Cu. The high-resolution Cu 2p spectrum (Figure 6b) exhibits the main $Cu2p_{3/2}$ peak at 934.8 eV and the $Cu2p_{1/2}$ peak at 954.7 eV, accompanied by strong satellite peaks. This spectral signature is characteristic of the Cu^{2+} oxidation state, confirming the integrity of the metal nodes within the MOF structure. The most insightful results were obtained from the high-resolution This provides direct spectroscopic evidence of a strong covalent/coordinative linkage between the MXene support and the MOF, which is crucial for efficient charge transfer and the overall stability of the hybrid [26].

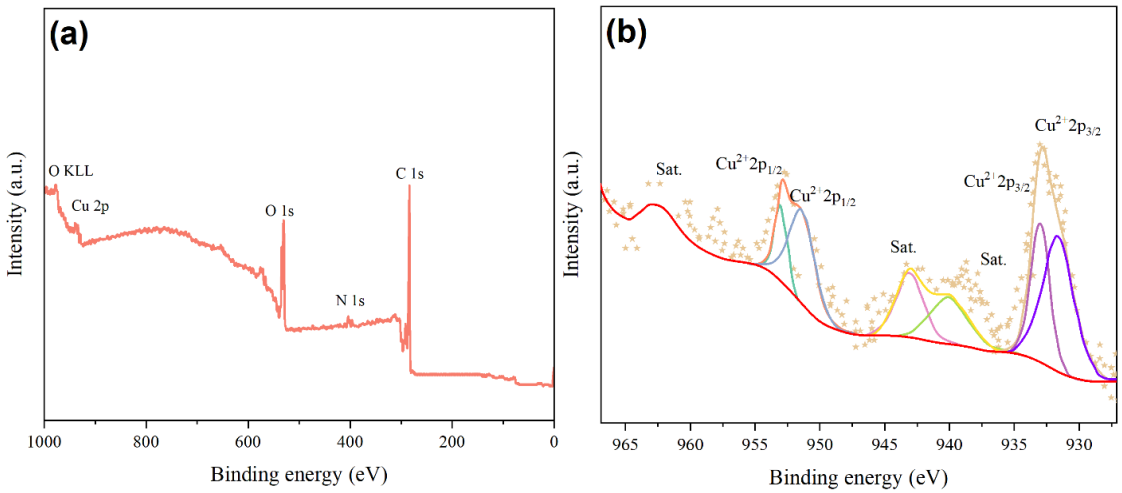

Fig. 6. XPS spectra of the MX-MOF hybrid: (a) survey scan, (b) Cu 2p region

Nitrogen adsorption–desorption analysis was conducted to evaluate the porosity and surface area of the prepared materials. The pristine Cu-BTC MOF displayed a representative Type I isotherm, confirming its microporous nature, and exhibited a Brunauer–Emmett–Teller (BET) specific surface area as high as 1350 m^2/g. In contrast, the delaminated $Ti_3C_2T_x$ nanosheets show a Type II isotherm with negligible N_2 uptake, indicating a non-porous nature and a low specific surface area of less than 20 m^2/g. The MX-MOF hybrid material displays a composite isotherm with features of both Type I and Type IV behavior, indicating the presence of both micropores (from the MOF) and mesopores (formed in the interstices between the MOF crystals and MXene sheets). The hybrid material demonstrates a substantial BET surface area of 820 m^2/g. This result is significant as it confirms that the hybridization process successfully preserves a large, accessible porous network, which is essential for allowing the efficient diffusion of substrates to the catalytically active sites within the MOF component.

3.3 Evaluation of Peroxidase-Like Activity

The peroxidase-like (POD-like) catalytic performance of the synthesized materials was assessed by examining their capacity to promote the H_2O_2-driven oxidation of TMB [27]. As illustrated by the time-resolved UV–vis absorption spectra in Figure 7a, the system containing the MX–MOF hybrid showed a pronounced and rapid rise in absorbance at 652 nm, corresponding to the characteristic signal of oxidized TMB (oxTMB). In contrast, the reactions catalyzed by pure MXene, pure Cu-BTC MOF, or a simple physical mixture of the two showed significantly slower rates of color development [28]. A quantitative comparison of the initial reaction rates (Figure 7b) reveals a remarkable synergistic catalytic enhancement in the hybrid material. The MX–MOF nanozyme exhibited catalytic performance that was nearly eight times greater than that of the pristine MOF and more than twenty times higher compared with the unmodified MXene. This pronounced enhancement underscores that the intimate interfacial connection established during the in situ synthesis is critical for the superior performance, far exceeding the simple additive effect of its components. The catalytic activity was found to be highly dependent on reaction conditions, with optimal performance observed at pH 4.0 and a temperature of 45 °C, as depicted in Figure 7c.

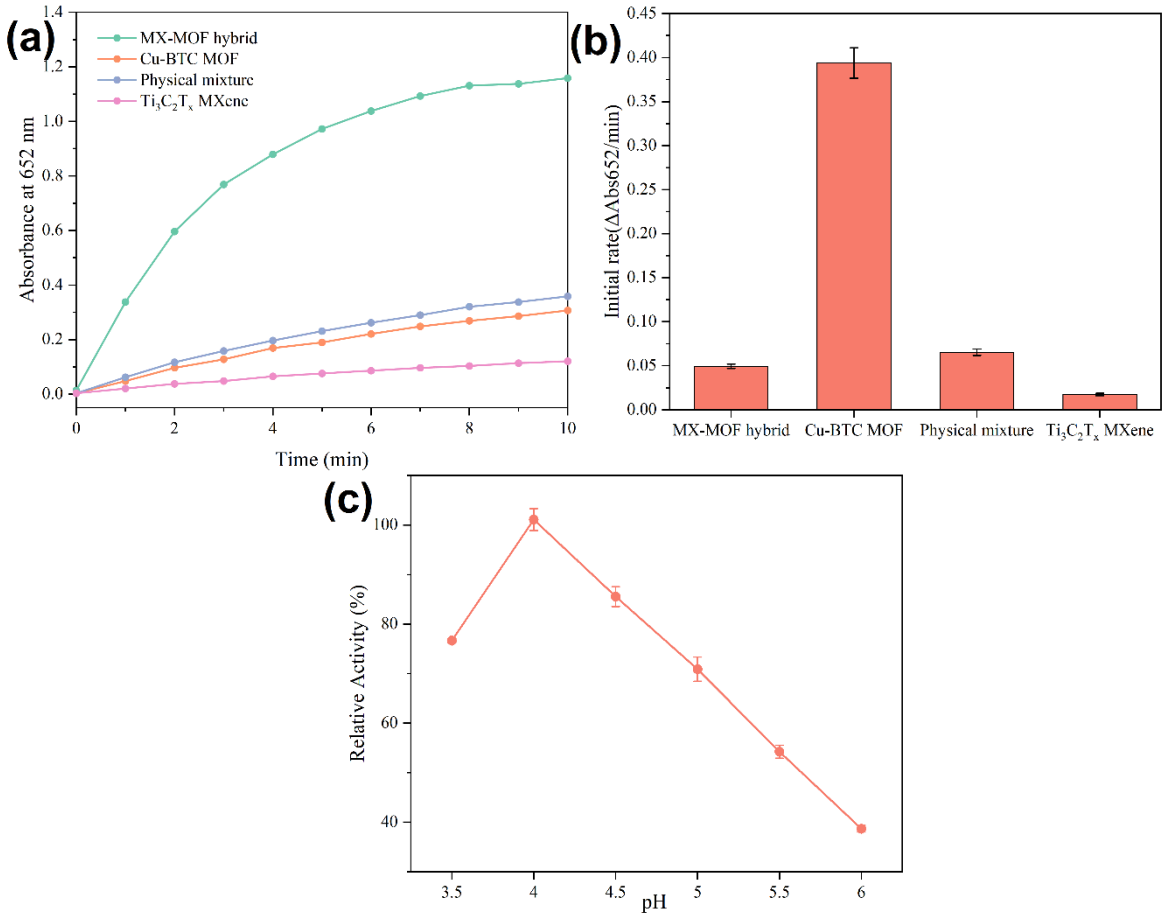

Fig. 7. Peroxidase-like catalytic performance of the MX-MOF hybrid compared with controls: (a) time-dependent UV–vis absorption spectra showing oxTMB formation at 652 nm; (b) comparison of initial reaction rates for MXene, Cu-BTC MOF, physical mixture, and MX-MOF hybrid; (c) effect of pH and temperature on the catalytic activity of the MX-MOF nanozyme.

To better elucidate the catalytic pathway and overall efficiency, steady-state kinetic analyses were carried out. In these experiments, the concentration of one substrate was systematically altered while the other was maintained at a fixed level, and the initial reaction velocities were subsequently recorded. The obtained data, presented as Michaelis–Menten plots (Figure 8a, 8b), exhibited the characteristic saturation behavior commonly observed in enzymatic systems. From the corresponding Lineweaver–Burk transformations (Figure 8c, 8d), the principal kinetic parameters—the Michaelis–Menten constant (Km) and the maximum reaction rate (Vmax)—were extracted. The MX-MOF nanozyme exhibited a Km value of 0.12 mM with respect to H_2O_2, a value that is more than 30 times lower than that of natural HRP (3.7 mM) [29]. This significantly lower Km indicates a much higher binding affinity of the nanozyme for the H_2O_2 substrate. This enhanced affinity is a critical advantage, particularly for biosensing applications involving cascade reactions where the intermediate species is generated at low concentrations. Furthermore, the Vmax value for the hybrid was substantially greater than that of its individual components, confirming its superior catalytic turnover rate and overall efficiency.

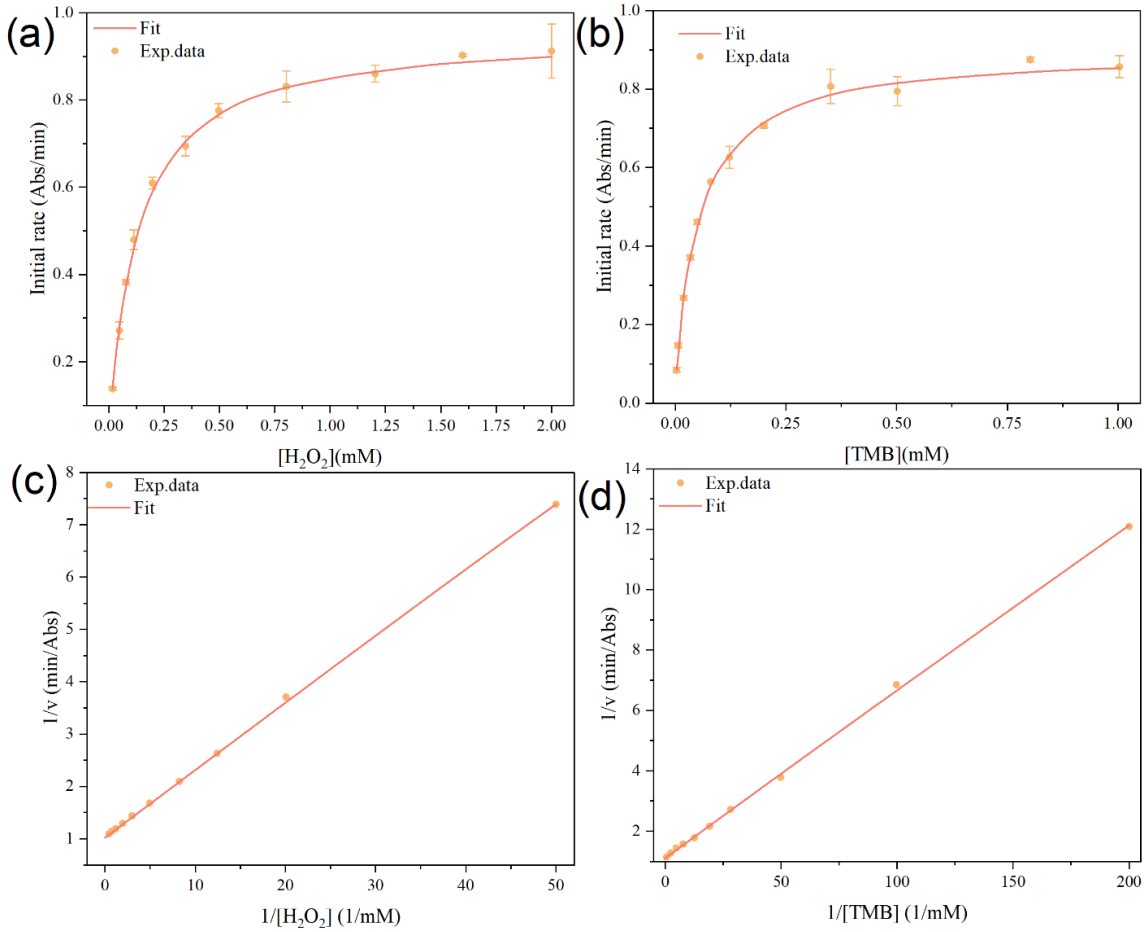

Fig. 8. Steady-state kinetic analysis of the MX-MOF nanozyme showing Michaelis–Menten curves for (a) H_2O_2 and (b) TMB substrates, and the corresponding Lineweaver–Burk plots.

Based on the characterization and kinetic results, a plausible mechanism for the synergistic catalysis is proposed and illustrated in Figure 9. The highly porous Cu-BTC MOF component provides a high density of catalytically active Cu2+ sites that are readily accessible to the substrates. The catalytic cycle begins with a Fenton-like reaction where H_2O_2 interacts with the copper centers [30]. The key step is the generation of highly reactive •OH, which are the primary oxidizing species responsible for the rapid oxidation of the TMB substrate to its colored product, oxTMB [31]. The rate-limiting step in many MOF-based nanozymes is the regeneration of the active metal species (i.e., the reduction of Cu^{2+} to Cu^{+}). It is proposed that the exceptional metallic conductivity of the underlying $Ti_3C_2T_x$ MXene support plays a crucial role here. The MXene nanosheets act as an "electron highway," providing a low-resistance pathway for electrons to be rapidly transferred from the TMB substrate to the Cu2+ active sites in the MOF. This facilitated electron transfer dramatically accelerates the Cu2+/Cu+ redox cycle, thereby boosting the overall rate of •OH generation and leading to the observed synergistic enhancement in catalytic activity. This mechanism effectively connects the unique material properties of the hybrid to its emergent high-performance catalytic function [32].

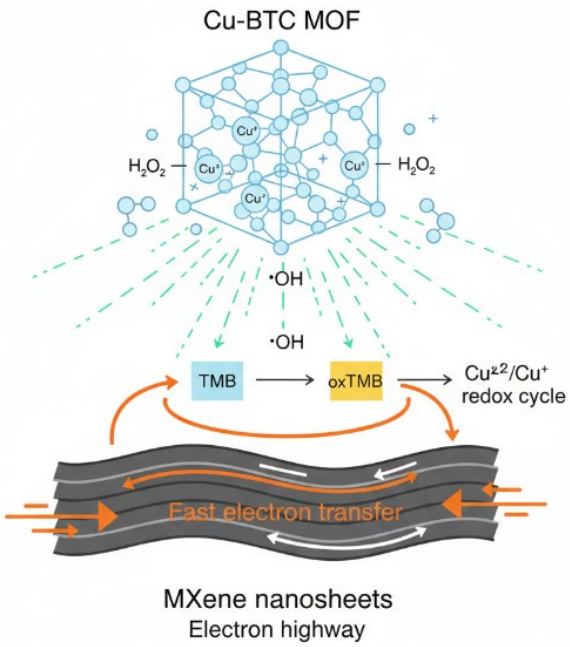

Fig 9. Proposed catalytic mechanism of the MX-MOF hybrid, where Cu^{2+} sites in the MOF generate reactive •OH species via a Fenton-like process, and the conductive MXene sheets facilitate rapid electron transfer to accelerate the Cu^{2+}/Cu^{+} redox cycle, leading to enhanced peroxidase-like activity.

3.4 Performance of the GNN-Designed Nanozyme for Glucose Biosensing

The superior peroxidase-like activity of the GNN-designed MX-MOF nanozyme was harnessed to develop a sensitive colorimetric assay for glucose [33]. The sensing strategy is based on a sequential two-enzyme cascade process [34]. Initially, glucose undergoes selective oxidation by GOx in the presence of molecular oxygen, producing gluconic acid along with H_2O_2. In the subsequent step, the MX–MOF nanozyme utilizes the in situ generated H_2O_2 to catalyze the transformation of the chromogenic substrate TMB from its colorless state into the oxidized blue product. The intensity of the developed blue coloration correlates linearly with the starting glucose concentration, thereby enabling quantitative detection. The feasibility of this cascade reaction was confirmed experimentally, where a significant increase in absorbance at 652 nm was observed only when both GOx and glucose were present in the system, demonstrating the specific detection pathway.

After fine-tuning critical experimental conditions, including the incubation duration of GOx and the amount of nanozyme employed, the glucose biosensor was subjected to a systematic assessment of its analytical performance. The addition of increasing concentrations of glucose to the assay system resulted in a visually discernible color gradient from colorless to deep blue (Figure 10a). The calibration plot displayed in Figure 10b illustrates the relationship between absorbance at 652 nm and glucose concentration. A well-defined linear dependence was observed across the range of 1.0 μM to 250 μM, yielding an excellent correlation coefficient of 0.998. The LOD was determined as 0.72 μM using the 3σ/S approach, where σ represents the standard deviation of the

blank measurements and S denotes the slope of the calibration curve. The combination of this broad linear range and remarkably low detection limit highlights the high sensitivity of the developed assay, confirming its suitability for accurate glucose determination in biological samples. The performance of the developed sensor is compared with other recently reported nanozyme-based glucose sensors in Table 1, highlighting its competitive or superior analytical figures of merit.

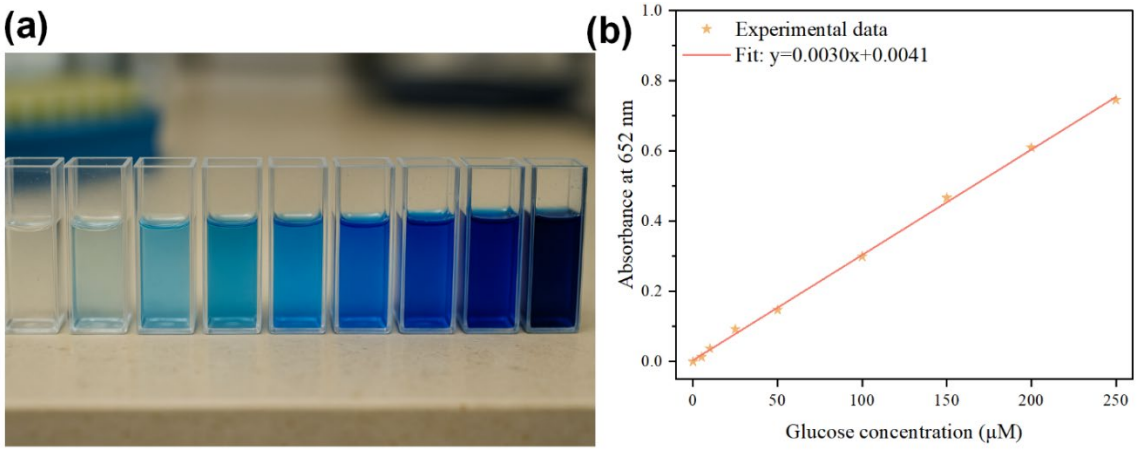

Fig. 10. Colorimetric glucose assay using the MX-MOF nanozyme: (a) color change with increasing glucose concentration; (b) calibration curve showing linear relationship between absorbance at 652 nm and glucose concentration.

Table 1. Comparison of the analytical performance of different nanozyme-based glucose sensors.

Nanozyme Material	Detection Method	Linear Range (μM)	LOD (μM)	Reference
GNN-designed MX-MOF	Colorimetric	1.0–250	0.72	This work
MXene-Ti_3C_2/Co NSs	Colorimetric	-	1.7	[35]
Cu-MOF	Colorimetric (Multi-enzyme system)	55–1665	-	[36]
NO_2-MIL-53(Cu)	Colorimetric	0.5–300	2.6	[37]
Cu_2O/MXene/AC	Electrochemical	4–13300	1.96	[38]
Pt/MXene	Electrochemical	0–8000	-	[39]

The selectivity of a biosensor is a critical parameter for its practical application. The selectivity of the proposed glucose assay was investigated by measuring the sensor's response to a 100 μM glucose solution in the presence of a 10-fold higher concentration (1 mM) of various potential interfering species commonly found in human serum. As shown in Figure 11a, common metabolites such as ascorbic acid (AA), uric acid (UA), fructose, and lactose, as well as common ions like Na^+, K^+, and Cl^-, produced a negligible change in the absorbance signal. This high

selectivity is primarily attributed to the specific enzymatic catalysis of glucose by GOx. Beyond evaluating selectivity, the durability of the nanozyme under prolonged storage was also investigated. An aqueous suspension of the MX–MOF nanozyme was kept at 4 °C, and its catalytic activity was monitored at regular intervals over a period of one month. The nanozyme retained over 95% of its initial activity after 30 days of storage (Figure 11b), demonstrating its exceptional robustness and stability compared to natural HRP, which often loses significant activity under similar conditions. The reproducibility of the assay was also excellent, with an RSD of less than 4% for five independent measurements of a 100 μM glucose sample.

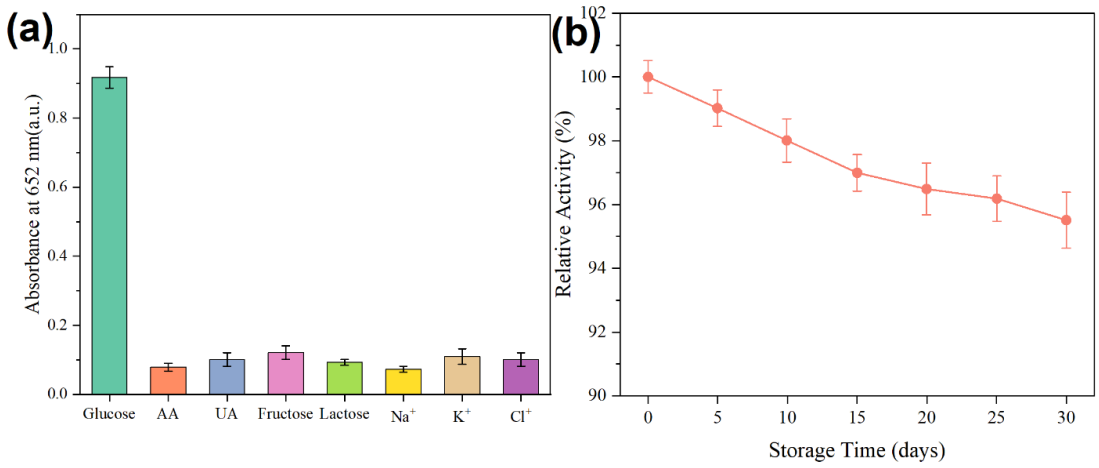

Fig. 11. Selectivity and stability of the MX-MOF-based glucose sensor: (a) response to glucose compared with common interfering species; (b) long-term storage stability over 30 days.

To validate the practical utility and accuracy of the developed biosensor for real-world applications, it was employed to determine the concentration of glucose in spiked human serum samples. To reduce potential matrix interferences, the serum specimens were initially diluted tenfold with PBS and subsequently fortified with predetermined amounts of glucose. These prepared samples were then subjected to analysis using the optimized colorimetric assay. The results, summarized in Table 2, show excellent recovery rates ranging from 97.2% to 104.5%, with RSD values all below 5%. Furthermore, the glucose concentrations determined by the nanozyme-based assay were in strong agreement with the values obtained using a commercial glucometer. This successful analysis in a complex biological matrix confirms the accuracy, reliability, and anti-interference capability of the GNN-designed MX-MOF nanozyme sensor, underscoring its significant potential for clinical diagnostics.

Table 2. Determination of glucose in spiked human serum samples (n = 3).

Sample No.	Spiked (μM)	Measured by Glucometer (μM)	Measured by this method (μM)	Recovery (%)	RSD (%)
1	0	95.5 ± 4.1	92.8 ± 3.5	-	3.8
2	50	146.2 ± 5.8	145.3 ± 6.1	104.5	4.2

3	100	194.8 ± 7.2	198.6 ± 8.3	101.9	4.2
4	200	296.1 ± 10.4	287.9 ± 11.5	97.2	4.0

4. Conclusion

A novel peroxidase-like nanozyme, composed of a Cu-BTC metal-organic framework grown in situ on delaminated Ti3C2Tx MXene nanosheets, was developed. The design of this optimal hybrid architecture was not the result of conventional trial-and-error experimentation but was intelligently guided by a pre-trained GNN model. Through this computational strategy, an extensive chemical space could be rapidly explored, leading to the identification of a candidate predicted to possess outstanding catalytic activity. This demonstrates an effective paradigm for expediting the discovery and rational design of next-generation functional materials. The resulting MX-MOF hybrid material exhibited exceptional catalytic performance, a direct consequence of the powerful synergistic effects between its components. The high metallic conductivity of the MXene scaffold was shown to facilitate rapid electron transfer, while the porous, high-surface-area MOF provided a dense population of accessible catalytic active sites. This unique combination led to superior catalytic kinetics, most notably a significantly higher substrate affinity (lower Km) for H_2O_2 compared to natural horseradish peroxidase. Upon incorporation into a biosensing system, the engineered nanozyme facilitated highly sensitive and selective colorimetric determination of glucose, achieving a remarkably low detection limit of 0.72 μM. Moreover, the platform exhibited outstanding accuracy and reproducibility when applied to complex biological environments, including human serum samples. The success of this GNN-directed methodology underscores the immense potential of integrating artificial intelligence with experimental materials science to overcome long-standing challenges in material design. The workflow presented here is not limited to nanozymes for biosensing but can be readily adapted to design a wide array of functional nanomaterials for diverse applications, including catalysts for sustainable energy conversion, materials for environmental remediation, and next-generation therapeutic agents. This research paves the way for a new era of intelligent, predictive, and rapid materials design, fundamentally changing the approach to creating materials with tailored, high-performance properties.

Availability of Data and Materials

The datasets used and analyzed during the current study are available from the corresponding author on reasonable request.

Author Contributions

F.F.T. conceptualized the study, designed the methodology, conducted the investigation, performed formal analysis, curated the data, and prepared the original draft of the manuscript. J.L.H. contributed to methodology optimization, data interpretation, visualization, and writing—review and editing. F.F.T. supervised the project, administered the research activities, and acquired funding. All authors have read and agreed to the published version of the manuscript.

Acknowledgements

None

Funding

This work has been supported by 2025 Science and Technology Plan Project of Taizhou (Research on key technologies for constructing novel biosensors, Grant No. 25gyb22); 2024 Research Launch Fund of Taizhou Vocational & Technical College (2024GCC06); 2024 Science and Technology Plan Project of Taizhou (Design and Development of Advanced Vehicle Controller for New Energy Vehicles, Grant No. 24gyb23); 2025 Research Project on Education Science Planning of Taizhou (Grant No. TZ25106).

Conflict of Interest

The authors declare no conflict of interest.

References

[1] C. P. Kurup, M. U. Ahmed, Biosensors 13, 461(2023).
https://doi.org/10.3390/bios13040461
[2] X. Yuan, X. He, J. Fan, Y. Tai, Y. Yao, Y. Luo, J. Chen, H. Luo, X. Zhou, F. Luo, Q. Niu, W. (Walter) Hu, X. Sun, B. Ying, Journal of Materials Chemistry B 13, 1599–1618(2025). https://doi.org/10.1039/D4TB02315C
[3] U. U. Rahman, M. Humayun, U. Ghani, M. Usman, H. Ullah, A. Khan, N. M. El-Metwaly, A. Khan, Molecules 27, 4909(2022).
https://doi.org/10.3390/molecules27154909
[4] M. Bosch, S. Yuan, W. Rutledge, H. -C. Zhou, Accounts of Chemical Research 50, 857–865(2017).
https://doi.org/10.1021/acs.accounts.6b00457
[5] A. Aldhaher, N. Rabiee, S. Iravani, Hybrid Advances 5, 100131(2024). https://doi.org/10.1016/j.hybadv.2023.100131
[6] H. Saini, N. Srinivasan, V. Šedajová, M. Majumder, D. P. Dubal, M. Otyepka, R. Zbořil, N. Kurra, R. A. Fischer, K. Jayaramulu, ACS Nano 15, 18742–18776(2021).
https://doi.org/10.1021/acsnano.1c06402
[7] S. Feng, S. Wen, R. Wang, X. Yang, X. Yuan, Y. Liu, J. Ma, Z. Li, Nanomaterials 15, 841(2025). https://doi.org/10.3390/nano15110841
[8] J. Cai, X. Chu, K. Xu, H. Li, J. Wei, Nanoscale Advances 2, 3115–3130(2020). https://doi.org/10.1039/D0NA00388C
[9] X. Shi, L. Zhou, Y. Huang, Y. Wu, Z. Hong, Materials Genome Engineering Advances 2, e50(2024).
https://doi.org/10.1002/mgea.50
[10] V. Bernales, M.A. Ortuño, D.G. Truhlar, C.J. Cramer, L. Gagliardi, ACS Central Science 4, 5–19(2018).
https://doi.org/10.1021/acscentsci.7b00500
[11] A. R. M. Silva, J. Y. N. H. Alexandre, J. E. S. Souza, J. G. L. Neto, P. G. de Sousa Júnior, M. V. P. Rocha, J. C. S. dos Santos, Molecules 27, 4529(2022).
https://doi.org/10.3390/molecules27144529

[12] Z. Wang, W. Li, S. Wang, X. Wang, WIREs Computational Molecular Science 15, e70010(2025). https://doi.org/10.1002/wcms.70010

[13] Q. -J. Hong, S. V. Ushakov, A. van de Walle, A. Navrotsky, Proceedings of the National Academy of Sciences of the United States of America 119, e2209630119(2022). https://doi.org/10.1073/pnas.2209630119

[14] V. Bhat, P. Sornberger, B. S. S. Pokuri, R. Duke, B. Ganapathysubramanian, C. Risko, Electronic, redox, Chemical Science 14, 203–213(2022). https://doi.org/10.1039/D2SC04676H

[15] S. Chakraborty, W. Xie, N. Mathews, M. Sherburne, R. Ahuja, M. Asta, S. G. Mhaisalkar, ACS Energy Letters 2, 837–845(2017). https://doi.org/10.1021/acsenergylett.7b00035

[16] M. Savage, Y. Cheng, T. L. Easun, J. E. Eyley, S. P. Argent, M. R. Warren, W. Lewis, C. Murray, C. C. Tang, M. D. Frogley, G. Cinque, J. Sun, S. Rudić, R. T. Murden, M. J. Benham, A. N. Fitch, A. J. Blake, A. J. Ramirez-Cuesta, S. Yang, M. Schröder, Advanced Materials 28, 8705–8711(2016). https://doi.org/10.1002/adma.201602338

[17] H. Demir, H. Daglar, H. C. Gulbalkan, G. O. Aksu, S. Keskin, Coordination Chemistry Reviews 484, 215112(2023). https://doi.org/10.1016/j.ccr.2023.215112

[18] N. Jahan, S. Hussain, H. U. Rahman, I. Manzoor, S. Pandey, K. Habib, S. K. Ali, R. Pandita, C. Upadhyay, Structural, Journal of Multidisciplinary Applied Natural Science 1, 13–17(2021). https://doi.org/10.47352/jmans.v1i1.6

[19] P. Nikhil, S. Sornambikai, G. Bhuvaneshwari, N. Ponpandian, C. Viswanathan, ACS Applied Electronic Materials 5, 5463–5476(2023). https://doi.org/10.1021/acsaelm.3c00681

[20] L. Biswal, B. P. Mishra, S. Das, L. Acharya, S. Nayak, K. Parida, Inorganic Chemistry 62, 7584–7597(2023). https://doi.org/10.1021/acs.inorgchem.3c01138

[21] L. Chen, B. Cui, C. Zhang, X. Hu, Y. Wang, G. Li, L. Chang, L. Liu, Environmental Science & Technology 58, 10558–10566(2024). https://doi.org/10.1021/acs.est.4c03478

[22] P. Bärmann, R. Nölle, V. Siozios, M. Ruttert, O. Guillon, M. Winter, J. Gonzalez-Julian, T. Placke, ACS Nano 15, 3295–3308(2021). https://doi.org/10.1021/acsnano.0c10153

[23] X. Liu, X. Wei, Z. Zhang, X. Wang, G. Liu, D. Luo, J. Li, Renewables 2, 162–170(2024). https://doi.org/10.31635/renewables.024.202400051

[24] H. Heydari, S. Salehian, S. Amiri, M. Soltanieh, S. A. Musavi, Polymer Testing 123, 108046(2023). https://doi.org/10.1016/j.polymertesting.2023.108046

[25] L. Wang, L. Song, Z. Yang, Y. -M. Chang, F. Hu, L. Li, L. Li, H. -Y. Chen, S. Peng, Advanced Functional Materials 33, 2210322(2023). https://doi.org/10.1002/adfm.202210322

[26] L. Lan, Z. -B. Fang, W. Deng, J. -D. Yi, R. Wang, T. -F. Liu, CCS Chemistry 4, 2782–2792(2021). https://doi.org/10.31635/ccschem.021.202101241

[27] C. Hong, X. Zhang, C. Wu, Q. Chen, H. Yang, D. Yang, Z. Huang, R. Cai, W. Tan, ACS Applied Materials & Interfaces 12, 54426–54432(2020).
https://doi.org/10.1021/acsami.0c15900
[28] W. -X. Jia, M. -M. Tao, X. -Y. Wang, Y. -F. Huang, Y. Li, Talanta Open 9, 100292(2024).
https://doi.org/10.1016/j.talo.2024.100292
[29] Q. Sun, J. Yu, R. Zhang, X. Yu, J. Xu, N. Niu, L. Chen, ACS Materials Letters 7, 646–653(2025).
https://doi.org/10.1021/acsmaterialslett.4c02563
[30] S. K. Padamati, T. A. Vedelaar, F. Perona Martínez, A. C. Nusantara, R. Schirhagl, Nanomaterials 12, 1422(2022).
https://doi.org/10.3390/nano12142422
[31] G. Li, H. Li, C. Wang, X. Li, J. Chen, J. Liang, Z. Zhou, IEEE Sensors Journal 23, 111–118(2023).
https://doi.org/10.1109/JSEN.2022.3224554
[32] P. Salarizadeh, M. B. Askari, A. Di Bartolomeo, ACS Applied Nano Materials 5, 3361–3373(2022).
https://doi.org/10.1021/acsanm.1c03946
[33] Y. Xia, F. Shi, R. Liu, H. Zhu, K. Liu, C. Ren, J. Li, Z. Yang, Analytical Chemistry 96, 1345–1353(2024).
https://doi.org/10.1021/acs.analchem.3c05053
[34] A. Márquez, S. Santiago, M. V. dos Santos, S. D. Aznar-Cervantes, C. Domínguez, F. G. Omenetto, G. Guirado, X. Muñoz-Berbel, ACS Applied Bio Materials 7, 853–862(2024).
https://doi.org/10.1021/acsabm.3c00872
[35] Z. Li, T. Lei, T. Pei, K. Chen, Z. Zhao, M. Wang, Y. He, Molecules 28, 5075(2023).
https://doi.org/10.3390/molecules28135075
[36] M. Lu, Z. Wang, W. Xie, Z. Zhang, L. Su, Z. Chen, Y. Xiong, Analytical and Bioanalytical Chemistry 415, 5949–5960(2023).
https://doi.org/10.1007/s00216-023-04844-y
[37] Y. Wang, Y. Wei, S. Li, G. Hu, Sensors 23, 6277(2023).
https://doi.org/10.3390/s23146277
[38] T. Selvi Gopal, J. T. James, B. Gunaseelan, K. Ramesh, V. Raghavan, C. J. Malathi A, K. Amarnath, V. G. Kumar, S. J. Rajasekaran, S. Pandiaraj, M. MR, S. Pitchaimuthu, C. Abeykoon, A. N. Alodhayb, A. N. Grace, ACS Omega 9, 8448–8456(2024).
https://doi.org/10.1021/acsomega.3c09659
[39] Q. -F. Li, X. Chen, H. Wang, M. Liu, H. -L. Peng, ACS Applied Materials & Interfaces 15, 13290–13298(2023).
https://doi.org/10.1021/acsami.2c20543